Ultramicroscopy 240 (2022) 113596

Contents lists available at ScienceDirect

Ultramicroscopy

journal homepage: www.elsevier.com/locate/ultramic

Strategy for optimizing experimental settings for studying low atomic number colloidal assemblies using liquid phase scanning transmission electron microscopy

Peter Kunnas [a,b], Mohammad-Amin Moradi [c], Nico Sommerdijk [d], Niels de Jonge [a,e,*]

[a] INM- Leibniz Institute for New Materials, Saarbrücken 66123, Germany
[b] Faculty of Physics, Quantum Imaging and Biophysics, University of Vienna, Vienna 1090, Austria
[c] Department of Chemical Engineering and Chemistry, Laboratory of Physical Chemistry, Eindhoven University of Technology, Eindhoven 5600 MB, the Netherlands
[d] Department of Biochemistry, Radboud University Medical Center, Nijmegen 6525 GA, the Netherlands
[e] Department of Physics, Saarland University, Saarbrücken 66123, Germany

A B S T R A C T

Observing processes of nanoscale materials of low atomic number is possible using liquid phase electron microscopy (LP-EM). However, the achievable spatial resolution (d) is limited by radiation damage. Here, we examine a strategy for optimizing LP-EM experiments based on an analytical model and experimental measurements, and develop a method for quantifying image quality at ultra low electron dose D_e using scanning transmission electron microscopy (STEM). As experimental test case we study the formation of a colloidal binary system containing 30 nm diameter SiO_2 nanoparticles (SiONPs), and 100 nm diameter polystyrene microspheres (PMs). We show that annular dark field (DF) STEM is preferred over bright field (BF) STEM for practical reasons. Precise knowledge of the material's density is crucial for the calculations in order to match experimental data. To calculate the detectability of nano-objects in an image, the Rose criterion for single pixels is expanded to a model of the signal to noise ratio obtained for multiple pixels spanning the image of an object. Using optimized settings, it is possible to visualize the radiation-sensitive, hierarchical low-Z binary structures, and identify both components.

1. Introduction

LP-EM [1–3] is capable of studying dynamic processes involving nano-scale objects such as nanoparticles (NPs) in a liquid layer of up to a few micrometers thickness. Since the first reported experiments [4], a common observation is that the Brownian-type motion of NPs blurs their appearance in LP-EM images [5] and sometimes causes them to move exceptionally slowly in a net direction [6]. Provided that contrast is sufficient, it is possible to analyze the dynamics of NPs with LP-EM to gain an insight into the forces affecting their behavior in a liquid environment [7–9]. NPs consisting of high atomic number materials such as Au, Pt, and Ti provide good contrast and have been used for LP-EM imaging with high resolution both in lateral and temporal terms [10–12]. For studies of soft matter containing low atomic number (Z) materials, the capabilities of dynamical LP-EM are limited due to contrast and radiation damage issues; this limits the spatial and temporal resolution when imaging, for example, colloidal suspensions [12–16]. Many examples exist of damage induced by the electron beam [17] as well as fading contrast of organic specimens [18]. In addition, artifacts have been reported to occur, such as metallic deposition [19] in the liquid cell, and the formation of globular, dendritic, and other types of structures in the solution due to the reduction of metallic ions [20]. Beam-induced formation of gas bubbles [21] may result in drastic changes in intensity and morphology due to the change in the sample thickness [22] and capillary forces, respectively. A typical observation is that the extent of beam-induced damage scales with the electron fluence (D_e), often termed as cumulative electron dose or just electron dose. It is defined as the number of electrons interacting with the observed section of the sample during an experiment. D_e affects both the quality of data and the structure of the observed object and is the key parameters for setting a balance for image contrast and electron beam damage when designing an experiment. Finally, the motion of nano-objects during exposure results in motion blur and can affect both the intensity and morphology observed in the final image. Therefore, the beam sensitivity of the sample components needs to be assessed in terms of structural damage, and motion blur.

Here, we examine a strategy for optimizing and measuring the performance of LP-EM in studying dynamic processes involving low-Z soft matter. As a case example, we visualize the structure and formation of colloidal binary particles [23] relevant for self-assembled hierarchical

* Corresponding author at: INM- Leibniz Institute for New Materials, Saarbrücken 66123, Germany.
E-mail address: niels.dejonge@leibniz-inm.de (N. de Jonge).

https://doi.org/10.1016/j.ultramic.2022.113596
Received 23 November 2021; Received in revised form 8 July 2022; Accepted 21 July 2022
Available online 23 July 2022

materials used, for example, in photonic applications [24] or as mesoporous catalyst supports [25]. The model system studied consists of positively charged, amino-functionalized, 30 nm-diameter, amorphous SiONPs, and negatively charged, 100 nm-diameter PMs. In buffers of low pH, they have been shown to organize into hierarchical binary structures where the SiONPs formed a shell around the PM [23].

Both polystyrene and SiO_2 are known to be rapidly affected by radiation damage [26,27] and it is necessary to define an acceptable D_e for the specific experimental conditions used in this work. To assess the acceptable D_e for imaging binary structures, the beam sensitivity of both components (SiONP and PM) will be determined by imaging the structure under increasing D_e, and then whole assemblies will be imaged under conditions compatible with both components

To minimize beam damage, the electron microscopy settings for image acquisition need to be optimized to maximize the amount of information per electron [28]. Theoretical calculations based on an analytical model of the resolution in LP-EM using STEM detection [29] are applied to examine what the optimal experimental parameters are for the aforementioned low-Z colloidal assemblies. Relevant experimental parameters studied are D_e, t of the liquid, detector opening angle (β), and blurring caused by the movement of the particles during the image acquisition. We also investigate the reliability of the theoretical predictions of image quality by testing the sensitivity of the calculations to changes in key experimental parameters including the material's density (ρ), and comparing calculated values with experimental data for practical imaging conditions. To quantitatively determine image quality in the noisy electron microscopic data, a method for image analysis was developed measuring visibility and experimental resolution of the NPs.

Finally, we test the possibility to directly visualize the hierarchical colloidal assemblies in dynamic conditions before radiation damage takes place.

2. Methods

2.1. Buffer and saline solutions

Phosphate buffered saline (PBS) with varying pH was prepared by mixing 1 M stock solutions (Table S1), then diluting to the final volume of 10 mL. The pH was determined with a digital pH meter (UltraBASIC, Denver Instruments, US). The 1 M stock solutions of NaCl (CELLPURE®, Carl ROTH, Germany) and NaH_2PO_4 were prepared by dissolving each salt in high-performance liquid chromatography (HPLC)-grade water (ROTISOLV®, Carl ROTH, Germany). 1 M stock solutions of NaOH (Fluka, Germany) and HCl (AppliChem, Germany) were used as acquired. Saline was prepared by diluting 440 μL of 1 M NaCl stock solution with HPLC-water to a total volume of 10 mL.

2.2. Colloidal dispersions

PMs in aqueous solution (Sigma-Aldrich, Germany) were used of a diameter of 109 ± 9 nm as measured manually from an SEM image of 10 dried PMs on a carbon grid (nominal magnification of 15,000 ×). The total solid content of the suspension was reported by manufacturer to be 10%, containing 0.1% sodium azide functioning as a preservative and surfactant. Before use, the PM solution was diluted to a volume ratio of 1:100 with PBS buffer of pH 2 and shaken.

As outlined by Yokoi et al., silica NPs were synthesized by dissolving 0.01 g of L-Lysine (Fluka, Germany) in 100 mL of distilled water and stirred with a speed of 270 rounds per minute (RPM) under reflux at 60°C [30]. To start the reaction, 6 mL of Tetraethylorthosilicate (TEOS) (VWR, US) was added and the mixture was left to react for 24 h at 60°C. Assuming all the TEOS reacted, the final concentration yield was 16.1 g l^{-1} for silica NPs. Averaging the diameters of 10 characterized SiONPs yielded 24 ± 3 nm, as measured manually from an image acquired after immobilizing the NPs on a SiN_x-membrane after which a STEM image was acquired at a nominal magnification of 400,000 × .

The surface of silica NPs was amino-functionalized based on a protocol described elsewhere [31]. Functionalization was accomplished with a 1:100 weight ratio of (3-aminopropyl)triethoxysilane (APTES) to the original amount of silica precursor (TEOS) used in the synthesis. The APTES was diluted to 4% (V/V) with tetrahydrofuran (THF), after which the desired amount was pipetted into a stirring sample of silica dispersion, which continued for 30 min. The SiONP suspension was diluted to a 1:5 volume ratio with PBS pH 2 and shaken before use.

The ζ-potential of 1:5 diluted SiONP was determined at pH values of 2, 7, and 12 and fixed ionic strength of 0.064 M. The measurement was taken with Malvern Zetasizer instrument (Malvern Panalytical Ltd, UK), and three measurements were conducted on each sample. Average measured ζ-potential values were 13 mV, -21 mV, and -38 mV for pH 2, 7, and 12, respectively.

To prepare pre-assembled binary structures *ex-situ* in bulk solution, 0.16 mL of SiONP suspension and 0.02 mL PM suspension (diluted 1:5 with HPLC-grade water) were added into 0.4 mL of 0.1 M KCL-HCL buffer of pH 1.6. The buffer was prepared by mixing 50 mL of 0.1 M KCl and 13 mL of 0.1 M HCL, resulting in a final pH of 1.6.

2.3. Calculations of dose-limited resolution

Numerical calculations to obtain attainable d for STEM in a liquid cell for polystyrene (C_8H_8) and amorphous silica (SiO_2) were performed according to the theory outlined in de Jonge et al. [29]. Mathematical equation-solving software (MATLAB, MathWorks, USA) see SI, Section 2.1 for the Matlab code) was used to calculate the numerical value of d, as has been done earlier for carbon and gold [29]. In short, the scattering properties of the sample components were obtained by calculating their average electron scattering cross section $\sigma(\theta)$ and the mean-free path length (l) for 200 keV electron energy (E). Physical parameters and microscopic parameters required for this calculation are reported in Matlab code section "Sample parameters" (SI, Section 2.1). The inelastic scattering component was included in the calculation of $\sigma(\theta)$ so that:

$$\sigma(\theta) = \sigma_{el}(\theta) + \sigma_{in}(\theta), \tag{1}$$

where $\sigma_{el}(\theta)$ and $\sigma_{in}(\theta)$ are the elastic and inelastic scattering cross-sections, respectively. In the case where only elastic scattering from the specimen was considered, the $\sigma_{in}(\theta)$ was set equal to zero.

To calculate the effective size of the electron probe that contained 50% of the incident electrons, first the diffraction-limited diameter of the electron probe (d_{50}) was calculated. The convergence semi-angle for the electron beam (α_p) was adjusted along with the detector's opening semi-angle (β). For DF-STEM, $\alpha_p = 8$ mrad if $\beta > 8$ mrad, and $\alpha_p = \beta/2$ when $\beta \leq 8$ mrad. For BF-STEM, $\alpha_p = 8$ mrad when $\beta < 8$ mrad and $\alpha_p = \beta$ when $\beta \leq 8$ mrad. Secondly, the probe broadening (d_{blur}) due to the scattering in the sample was obtained. Finally, to obtain the signal-to-noise limited resolution (d_{SNR}) for BF- and DF-STEM, the number of electrons hitting the detector at different sample locations was calculated.

For example, in the case of BF-STEM, the number of transmitted electrons at a position of water (M_{bkg}), and a nano-object (M_{signal}) was calculated using Eqs. (2) and (3), respectively.

$$M_{\mathrm{bkg}} = N_0\, \mathrm{e}^{-\frac{t}{l_{\mathrm{H2O}}} - \frac{2\,t_{\mathrm{SiN}}}{l_{\mathrm{SiN}}}} \tag{2}$$

$$M_{\mathrm{signal}} = N_0 \mathrm{e}^{\frac{d-t}{l_{\mathrm{H2O}}} - \frac{2\,t_{\mathrm{SiN}}}{l_{\mathrm{SiN}}} - \frac{d}{l_0}}, \tag{3}$$

where l_{H2O}, l_{SiN}, and l_o are the mean-free path lengths for water, SiN_x-membrane, and the nano-object, respectively. N_o is the number of incident electrons and d is the effective diameter of the spherical nano-object. The SNR at the location of the nano-object is obtained by:

$$SNR = \frac{M_{\mathrm{signal}} - M_{bkg}}{\sqrt{M_{bkg}}} > 3 \tag{4}$$

The electron dose used for an optimally sampled nano-object [29] is given by:

$$D_e = \frac{4N_0}{d_{SNR}^2} \quad (5)$$

The value for the *SNR* was set to satisfy the Rose-criterion of $SNR \geq 3$ and Eqs. (2)–(5) were solved numerically for d_{SNR} by using the vpasolve function in MATLAB. For polystyrene, the numerically solved value of d_{snr} was found to be negative for $\beta \gtrapprox 10$ mrad. For these values, $\mid d_{snr} \mid$ was plotted instead. We suspected that the negative value was due to the inversion of the contrast between the nano-object and the liquid background. This was confirmed for DF-STEM by separately calculating the M_{signal} and M_{bkg} and using the numerically solved value of d_{SNR} as the diameter of the polystyrene nano-object. The result indicates that indeed the ratio M_{signal}/M_{bkg} became < 1 at $\beta = 11$ mrad and therefore explains why the numerical solution of d_{SNR} is negative for values $\beta \gtrapprox 10$ mrad.

Finally, to obtain value for *d,* resolution-limiting terms were summed in quadrature [32]:

$$d = \sqrt{(2d_{50})^2 + d_{\mathrm{SNR}}^2 + d_{\mathrm{blur}}^2} \quad (6)$$

2.4. Scanning transmission electron microscopy (STEM)

STEM was conducted using a probe-corrected transmission electron microscope (ARM200CF, JEOL, Japan) at $E = 200$ keV. The pixel dwell time (τ) was in the range of 1–20 μs, and pixel size (s) was in the range of 3.3–3.8 nm, corresponding to the nominal magnification of the microscope of 60,000 × and 50,000 ×, respectively. The annular DF detector collection angle was set to either $\beta_{in} - \beta_{out} = 27$–110, 54–220, or 68–280 mrad. The probe convergence angle amounted to 13.4 mrad when a 20 μm condenser lens aperture (CLA) was used. A spot size of 4C was selected so that the probe current (I_p) was 81 pA. The I_p was measured by directly imaging the probe with the camera (Ultrascan 1000XP, Gatan, CA, USA) for which the conversion factor (9.9 counts per e^-) was determined with the built-in pico-amperemeter of the fluorescent screen as described in Keskin and de Jonge [18]. The error of the beam current measurement was estimated to be ±10%. To calculate the total D_e deposited per areal unit A per frame, the following equation was used:

$$D_e = \frac{I_p}{\mathrm{e}s^2\,\tau}, \quad (7)$$

where e is the elemental charge. The typical D_e used for STEM imaging in the liquid was in the range of 0.5–5.0 $e^-Å^{-2}$ per frame, and typically a sequence of 20–100 frames was acquired from the same area.

2.5. Liquid phase electron microscopy (LP-EM)

LP-EM experiments were performed with a dedicated liquid cell specimen holder (Ocean, DENSsolutions, Netherlands). Before experiments, the system was cleaned by flushing it with 200–400 μL of HPLC-grade ethanol, followed by HPLC-water, and an injection of air to remove most of the liquid. O-rings were removed, and the holder tip was cleaned with an HPLC-grade ethanol-soaked, lint-free tissue using pointy plastic tweezers. The O-rings and the holder tip were sonicated for 2 min in 50 mL of HPLC-grade ethanol- and HPLC-grade water. The tip was blow-dried with a stream of argon, and vacuum grease was applied to the O-rings to secure the tightness of the cell. To remove the photoresist from the microchips supporting the SiN_x-windows (DENSsolutions, Netherlands) the windows were cleaned by gently swirling in 50 mL of HPLC-grade acetone and HPLC-grade ethanol, respectively [33]. The microchips were then plasma-cleaned for 5 min with a power of 50 W in Ar/O_2-mixture (75%/25%) in a chamber that was first evacuated to a vacuum of 70 mTorr. (Solaris, Gatan, CA, US). In order to maintain control over t, and to protect the sample from compression during the loading, a bottom microchip with a 200 nm-thick spacer was used.

In this work, we created monolayers of nano-objects on the top of the window to study the experimental SNR and beam effects as a function of the D_e This procedure is preferred over loading the entirely filled liquid cell, as it ensures that only a monolayer of hydrated PMs exists in the upper window of the liquid cell.

2.5.1. SiONP monolayer

A monolayer of SiONP was deposited on the top window (no spacer) by first firmly pressing the vacuum-facing side of the microchip against the adhesive surface of a gel box and pipetting 0.5 μL of dispersion SiONP on it. After 1–2 min of incubation time, the microchip was washed 3–5 times with 500 μL of water and blotted dry on a lint-free tissue. The sample is enclosed in the liquid cell and first examined at ambient conditions with DF-STEM. The average t/l_{in} of the dry cell was 0.75 +/- 0.03 for 60 data points, matching the expected $t = 0.10$ μm of SiN_x of 0.74. The liquid is subsequently introduced to the system by applying liquid flow until the liquid fills the whole field of view. The average t/l_{in} is measured with the EELS log-ratio-technique (see Section 2.7), resulting in 3.5 ± 0.8, which corresponds to 0.5 ± 0.1 μm liquid after subtracting the contribution of windows (Eq. (8)). The bulging of the windows is observed as the liquid thickness at the edge is 0.4 μm and at the middle of the cell 0.7 μm.

2.5.2. PM monolayer

A monolayer of PMs was prepared similarly, but only a small ~0.1 μL droplet was applied to the window area, and after 30–60 s, the whole microchip was rinsed in a 50 mL bath of HPLC-water. After blotting the vacuum side of the microchip, a small droplet of water resided on the area where the drop of PM had resided, and the liquid cell was assembled and sealed immediately to prevent the PMs from drying. To experimentally test LP-EM of PM, a sample was prepared to contain PM immobilized on the top SiN window of the liquid cell, such as to achieve the highest possible d in STEM mode.

For the PM sample, the presence of the nanoparticles was verified from a STEM overview image (data not shown). The thickness of the non-filled liquid cell was then measured using EELS. A line scan was acquired of a length of 8.1 μm from the edge of the window in a region with water and single PM particles. The measured t/l_{in} did not increase towards the center of the window as is typically the case for a completely filled liquid cell [34]. The average t/l_{in} amounted to 1.21 +/- 0.02 for 79 data points, corresponding to $t = 83 \pm 3$ nm accounting for two SiN windows (Eq. (8)). It is likely that the liquid cell was only partly filled or affected by the Laplace pressure resisting the outward bulging of the membranes due to the residual water film at the hydrophilic SiN window [35]. A series of 50 DF-STEM images at $D_e = 0.46 \pm 0.05$ $e^-Å^{-2}$ per image (resulting in a total of $D_e = 23 \pm 2$ $e^-Å^{-2}$) allowed us to determine the radiation limit in D_e for a very thin liquid layer.

To examine the acceptable D_e for LP-EM of PM in thicker liquids, we connected the liquid cell to a liquid flow via a syringe pump and inject PBS of pH 2 into the area of the SiN window. This was done at a different sample position than for Fig. 3a. The average t across the field of view was measured with EELS as $t/l_{in} = 4.3 \pm 0.2$ for 36 data points which is equivalent to 0.63 ± 0.03 μm of water, somewhat thicker than at the edge due to window bulging. A stack of 27 images was acquired at $D_e = 1.9 \pm 0.2$ $e^-Å^{-2}$, with D_e at the very limit of detection, so that the cumulative D_e amounted to 51 ± 5 $e^-Å^{-2}$.

We also tested if the PM structure changes when the cell was filled with an ambient atmosphere by studying an air-dried PM sample in a sealed liquid cell. The air-dried sample showed a thin water layer of $t = 8 \pm 1$ nm as concluded from EELS ($t/\lambda = 0.78 \pm 0.1$). For this scenario, a sequence of 80 images acquired at an unexposed region results in a total $D_e = 37.1 \pm 0.4$ $e^-Å^{-2}$ when using $l = 3.3$ nm and $\tau = 1$ μs. Again, a running average of five consecutive frames was created from the data before it feeding it to the data analysis pipeline (see SI, Section 3.1).

To observe air-dried PMs, the small drop of residual water after

rinsing was left to dry for 2–3 min before assembling the cell.

2.5.3. Binary monolayer

To study the structural detail of self-organized binary structures, the suspension was diluted 1:10 with HPLC-water, and 2 μl of the mixture was directly loaded into the liquid cell by pipetting it on a plasma cleaned microchip. No spacer was used. Measurement of the average thickness of the cell yielded $t/l_{in} = 3.97$ corresponding to $t = 0.57 \pm 0.11$ nm.

2.6. Measurement of liquid thickness

To determine the presence of the liquid and measure t, electron energy loss spectroscopy (EELS) via the log-ratio technique [36] was used to provide the relative sample thickness (t/l_{in}), with l_{in} the inelastic mean free path length of the sample. Values of SiN_x ($l_{in,SiN} = 136$ nm), and water ($l_{in,\ H2O} = 175$ nm) were obtained as described elsewhere [37]. Settings used for the acquisition of the EEL spectra were $\alpha_p = 13.4$ mrad, EELS acceptance semi-angle of 20.8 mrad, and a spectrometer dispersion of 0.5 eV/channel. This allowed electrons to be effectively collected up to the electron energy loss of 860 eV. Using the line scan tool of the scan-control software (Digital Micrograph-3, Gatan, CA, USA), EELS spectra were collected across the field of view. The built-in function of the software was used to calculate t/l. To finally obtain t of the liquid (water), the contribution of windows was subtracted as was done in Jungjohann et al. [37]:

$$t_{H2O} = \left(t/l_{in} - \frac{t_{SiN}}{l_{in,SiN}} \right) \cdot l_{in,H2O} \tag{8}$$

The accuracy of this calculation is estimated to be ± 20% [36], whereby the main source of error is the estimation of l_{in}.

2.7. Image analysis

Image processing software (ImageJ) was used for image analysis in combination with graph plotting and statistical analysis software (Prism v. 7.03, GraphPad, San Diego, US). Simulated image data was analyzed by measuring the intensity and standard deviation values of the image signal from the indicated parts of images (PM, SiONP, and background). The lateral drift present in the experimental data was removed by using CVmatch Template ImageJ plugin. In more detail, a square with 100–300 pixels side length was drawn around a bright feature (e.g., salt deposit at the window), and subsequent frames were aligned relative to each other. The “Rigid”-model of the Cvmatch Template plugin was enabled to restrain the manipulation of aligned frames to translation in x- and y-directions in one-pixel steps only. In some cases, no suitable high-contrast features were present in the field of view, and low-contrast features of interest were not correctly recognized by the automatic alignment algorithm. In such a case, the manual alignment tool included in the TrackEM2-plugin of ImageJ was used. To manually align a stack, “landmarks” were placed on a feature (e.g., SiONP on the window) that was assumed to stay stationary for the duration of the image sequence. Next, the algorithm aligned the stack based on the location of landmarks using the “Rigid”-model and one-pixel step length.

To improve the *SNR* in a sequence of images, a “running” average was created from the aligned stack of images. For this, we used a custom-made script for ImageJ that averaged a given number of successive images in a stack.

The image processing pipeline used to analyze the size distribution of PMs is described in detail in SI, Section 3.1 and the ImageJ script is presented in SI, Section 3.2.

3. Results

3.1. Identifying the key experimental parameters for DF-STEM

For LP-EM of samples sensitive to radiation damage, it is crucial to optimize the experimental parameters for an optimal balance between d as low as possible, D_e below the limit of radiation damage, and t sufficiently large to enclose the sample and allow liquid flow. To aid optimization, we use analytical equations [29] to evaluate the influence of the above parameters for liquid-phase STEM of NPs of amorphous silicon dioxide and polystyrene. It is assumed that the NPs are immobilized on the upper liquid enclosing window with respect to a downward electron beam, and that the NPs are imaged in focus. Fig. 1a and b show d for polystyrene in BF- and DF-STEM, respectively.

BF imaging is advantageous at low D_e while BF and DF perform approximately the same way at the tested values of D_e. In both cases, the curve of d shows two minima, which is due to the inversion of contrast when decreasing β. Fig. 1c and d show the results for silica. Here, BF- and DF-STEM perform almost the same at their respective optimal β, and contrast reversal is not observed.

For polystyrene the best theoretical resolution is obtained with DF-STEM and for silica with BF-STEM. From a practical point of view, however, the differences between results obtained with DF and BF are small for optimal β. For example, when comparing attainable resolution between DF and BF for $t = 300$ nm and $D_e = 10\ e^{-}Å^{-2}$, the differences in d are 0.7% and 11% for polystyrene and silica, respectively.

However, for β above its optimal value, DF-STEM is less sensitive to variation of β (Fig. 1b and d) than BF-STEM, and thus DF-STEM is less sensitive to the exact setting of β (Fig. 1a and c). Therefore, experimentally DF-STEM is preferred here over BF-STEM. For $D_e = 10\ e^{-}Å^{-2}$, it can be expected that the used NPs are visible in the images, i.e. the respective values of d for PM and SiONP are each a factor of two better than needed to detect the NPs used in the experiment, which have diameters of 109 and 24 nm, respectively.

The difference in the performance of DF-STEM and BF-STEM arises from the fact that in DF-STEM, the total number of electrons landing on the detector is greater which, according to Poisson statistics, leads to higher standard deviation (nominator in Eq. (5)) and thus lower SNR and worse achievable resolution.

The above calculations depend on the exact knowledge of several experimental parameters. However, there is always a certain degree of uncertainty related to the experimental parameters leading to different values of d. To double-check the validity of the calculations regarding the experiment, d is evaluated in relation to those experimental parameters that exhibit the largest degree of uncertainty. The first source of uncertainty in the calculated d originates from the accuracy of 10% in determining D_e. But this inaccuracy is negligible compared to two other factors (Fig. 2). Due to the bulging of the liquid-enclosing windows and measurement inaccuracy, t may be known in an experiment with an accuracy of a factor of two only. Yet, for our experimental setting of $t =$ 300 nm, t only exerts a moderate effect on d when an optimal β is used. Note that while an effective reduction of t would be achieved by using graphene sheets instead of silicon nitride windows to enclose the liquid [38,39], the gain would not be large for this range of t and d. Finally, we evaluate the uncertainty related to the density of the amorphous silica (ρ_{SiO2}) [40]. Here, the value of $\rho_{SiO2} = 1640\ kg/m^3$ is used, which was obtained using analytical centrifugation of another silica NP batch synthesized with the same parameters [40]. However, depending on the synthesis method, size, and degree of crystallinity, ρ_{SiO2} is in the range of 1370–2650 kg/m^3, and this uncertainty in ρ_{SiO2} in turn has a major influence on D_e (Fig. 1a), much more so than varying t and D_e. In the worst-case scenario, the calculated d is off by 50% but this is still sufficient to optimize the experiment. For example, the trend as a function of β is present regardless a shift in ρ_{SiO2}.

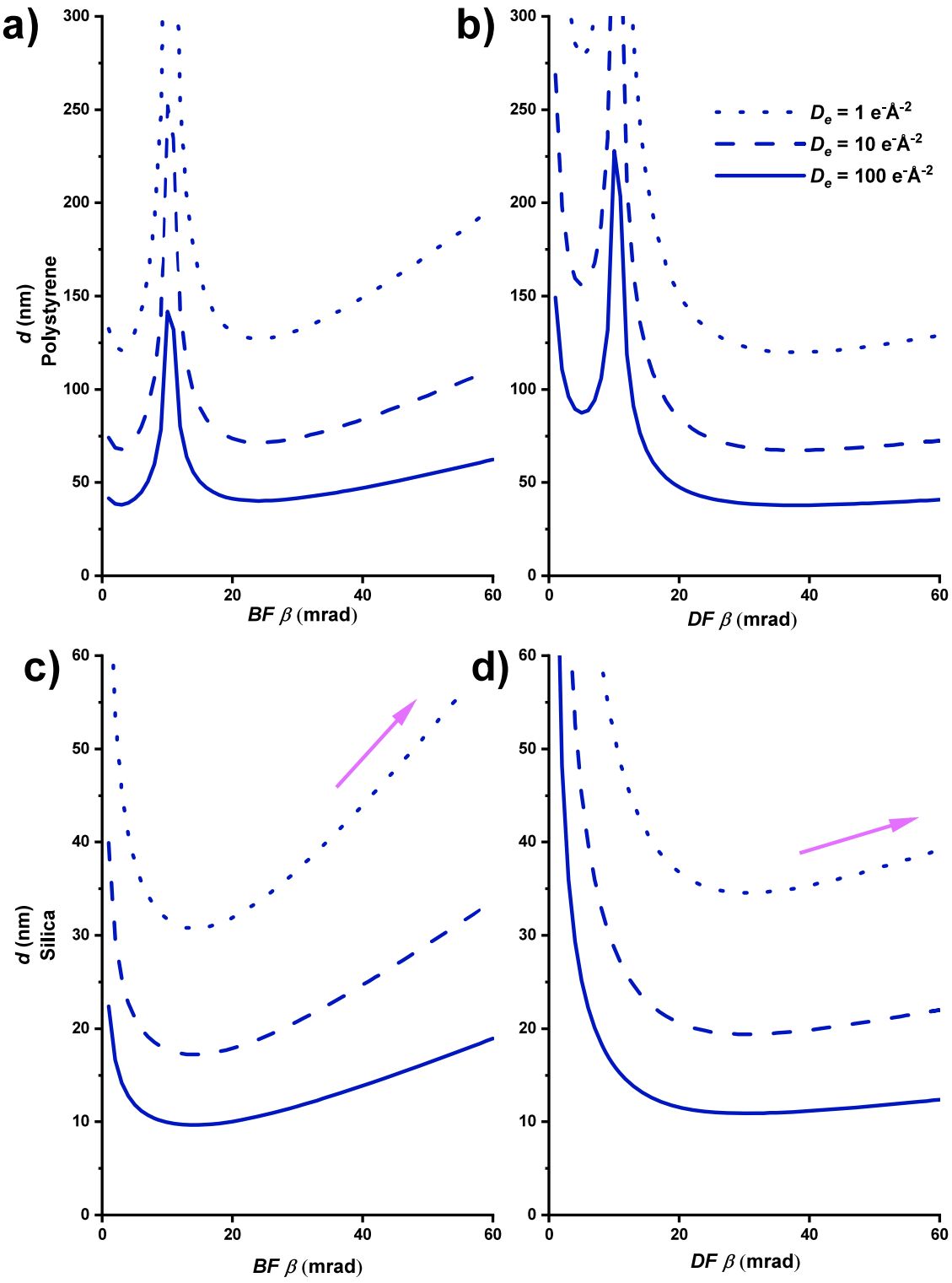

Fig. 1. Calculated attainable resolution d for polystyrene (a,b) and silica (c,d) in bright-field (BF) and dark-field (DF) scanning transmission electron microscopy (STEM) in liquid. The attainable resolution is calculated as a function of detector opening semi-angle (β) and electron dose (D_e) for liquid thickness $t = 300$ nm and silicon nitride thickness $t_{SiN} = 50$ nm. Arrows indicate the relative sensitivity of d when changing β while using BF and DF-STEM detection.

3.2. Structural beam sensitivity of PM

The key experimental question we address is whether the electron dose D_e needed for resolving the nanoparticles in liquid is below the limit of radiation damage of the studied materials. In particular, PM is expected to be sensitive to electron beam irradiation and we set out to study the effect of the electron beam on the appearance of the PM monolayer during the acquisition of a low dose image series in varying liquid thicknesses at $t = 0.008$, 0.084, and 0.65 μm. Fig. 3a. offers a qualitative observation of the beam-induced damage where PM monolayer was pre-irradiated with D_e of 41.8 $e^{-}Å^{-2}$ at $t = 84$ nm. The electron beam resulted in the removal of PMs in the pre-irradiated area as shown in the lower part of the panel a. In addition, At the edge of the irradiated area, smaller and fainter visible PM indicates partial removal of the NP

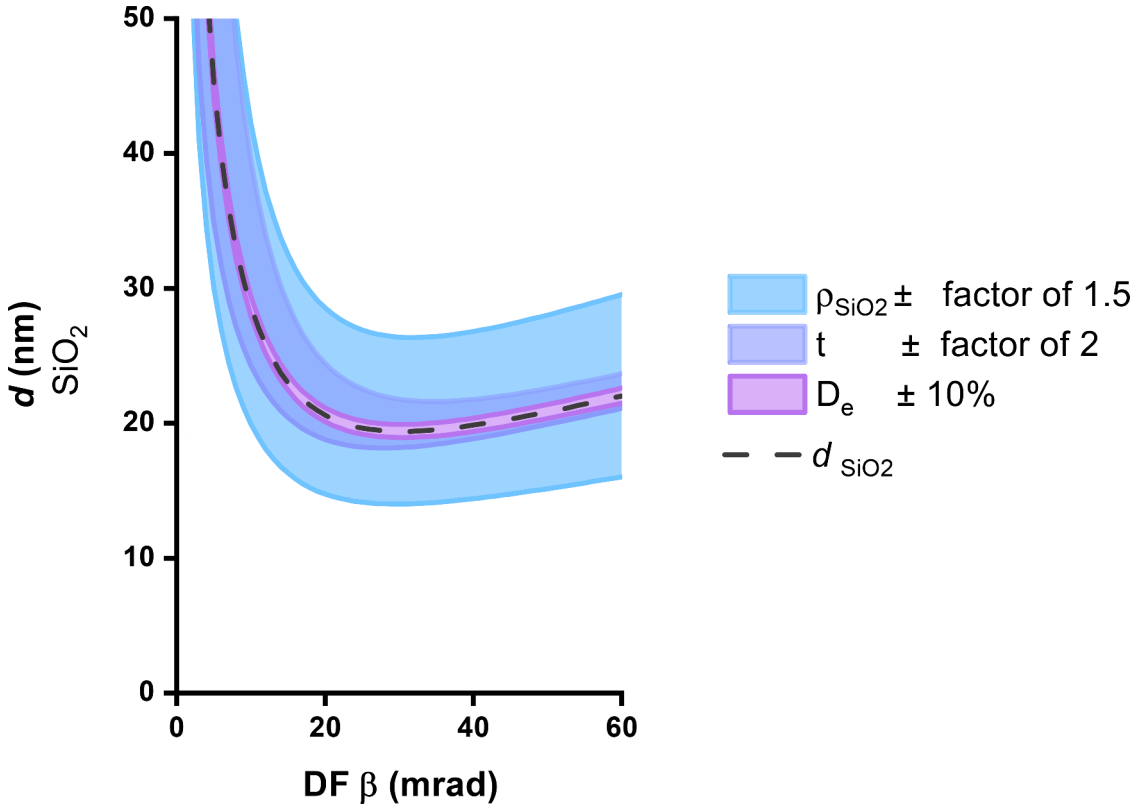

Fig. 2. Calculated tolerances of three parameters in attaining d, including the influence of adjusting the density of silica (ρ_{SiO2}), D_e, and t from the nominal values of 1.64 kg/m^3, 10 e$^-$Å^{-2}, and 300 nm, respectively.

structure. The latter observation shows that PM does not disappear as a whole but disintegrates while still attached to the liquid-solid interface, i.e. degradation of the material occurs.

Because structural degradation of PM would affect any measurement, it is important to determine the relationship between D_e and the size of the PM. This is achieved by analyzing both the image series in a thin liquid and the one in a thicker liquid (Fig. 3a and b). The PM diameter is measured in the individual images obtained for the thin liquid cell (Fig. 4a) from the full width of half maximum (FWHM) of a line over the NP location. The diameters of the NPs are automatically measured in a procedure involving detection, segmentation, and measuring projected areas (SI, Section 3.1). For the data in thicker liquid, this is impossible due to the low inherent contrast of PM, resulting in noisy data. Hence, the size distribution obtained from several PMs is evaluated as a function of D_e in order to increase the accuracy of the analysis. Secondly, the *SNR* of the data is improved by computing running averages of five consecutive frames in an image stack, resulting in an effective D_e of 2.3 ± 0.3 e$^-$Å^{-2} per frame. This averaging procedure results in a reasonable trade-off between *SNR* and the number of remaining data points. These data are filtered using a bandpass filter. As shown in Fig. 3c, the bandpass filtering improves the visibility of the PMs' outline. Finally, the nanoparticles are automatically detected and segmented (Fig. 3d).

In Fig. 3e, the determined size distribution of PMs in liquid of t = 0.63 μm is plotted for different values of D_e. It can be seen that the average diameter of the particles decreases, indicating structural degradation due to electron irradiation. A one-way analysis of variance (ANOVA) between the datasets of $D_e = 9.3 \pm 1$ e$^-$Å^{-2} and $D_e = 27.9 \pm 3$ e$^-$Å^{-2} indeed reveals a statistically significant change in the analyzed population of 160 PMs. No significant change is observed between D_e = 9.3 ± 1 e$^-$Å^{-2} and D_e = 18.6 ± 2 e$^-$Å^{-2}. This result indicates that significantly detectable electron beam damage takes place above the critical threshold of $D_e = 18.6 \pm 2$ e$^-$Å^{-2}

The result of this air versus liquid comparison is shown in Fig. 3f, where the measured average PM diameter under three different experimental conditions is plotted as a function of D_e. Structural degradation of PMs is faster in liquid than in the air atmosphere. Moreover, the degradation is more rapid in $t = 0.083$ μm than in $t = 0.63 \pm 0.03$ μm. The information provided in Fig. 3f can be used to estimate the degradation-induced change in the diameter of the PM for a given dose history and experimental setting. For example, in the case of $t = 0.63 \pm 0.03$ μm, $D_e = 37.2 \pm 4$ e$^-$Å^{-2} leads to a 10% reduction of the average diameter of the PM compared to the first image.

3.3. Resolving nano-objects in liquid

To support future measurements involving these radiation-sensitive low-Z materials, we calibrate the calculations with experimental LP-EM results in order to make realistic predictions of the achievable *SNR* and d for a given D_e and sample geometry. We do so by looking at two data sets; one for PMs and one for SiONPs.

PMs immobilized on the window and imaged at $D_e = 20 \pm 2$ e$^-$Å^{-2} are shown in Fig. 4a, where 11 frames are averaged from the dataset shown in Fig. 3b. Fig. 4d shows a sample containing an immobilized monolayer of SiONP on the upper window. A total of ten STEM images are acquired using $D_e = 4.6 \pm 0.5$ e$^-$Å^{-2} per image. The first image of the series is shown in Fig. 4c, revealing individual SiONPs. Due to the continuous operation of the scanning unit, the total irradiation of the sample is higher than 23 ± 2 e$^-$Å^{-2} as only every second frame is recorded in continuous acquisition mode. Based on the elapsed time between the captured frames (10.48 s) and the set flyback time (10 ms), the total D_e experienced by the sample is calculated to be a factor of two higher. Images are manually aligned and averaged cumulatively to obtain an image stack in which each consecutive frame is acquired with a higher D_e. During image acquisition, no movement or changes in the intensity are observed.

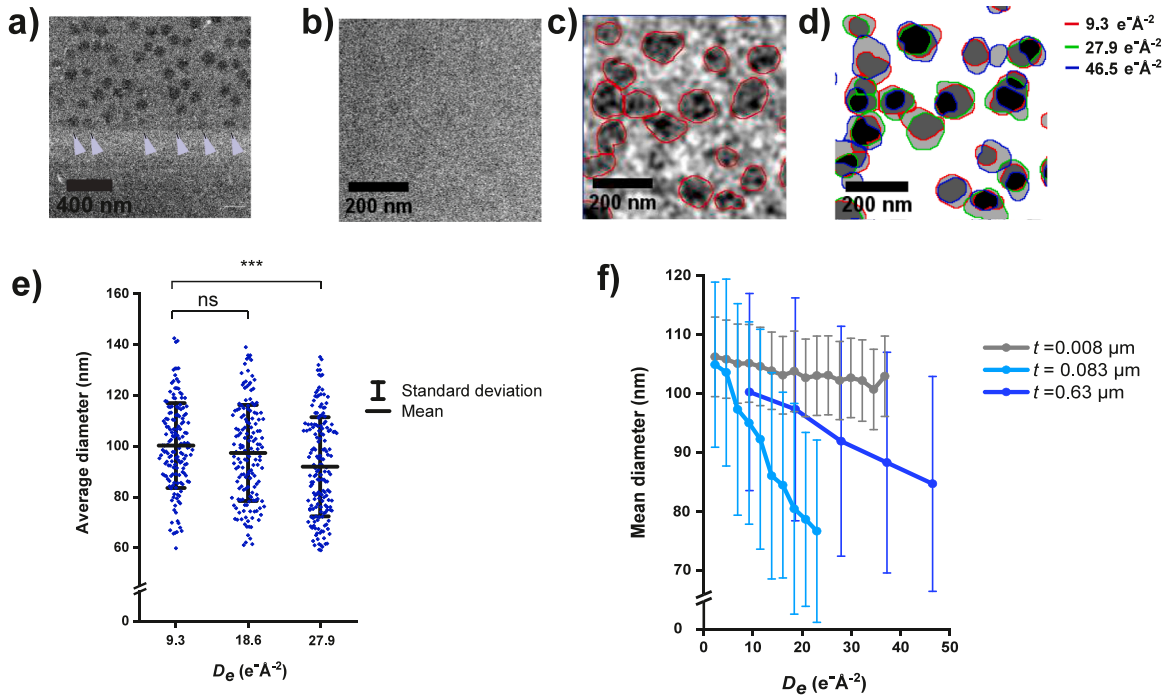

Fig. 3. Electron-beam-induced structural degradation of PM in liquid and air using microscope settings $\alpha_p = 13.4$ mrad, $\beta = 54$ mrad, $\tau = 1$–20 µs, and $s = 3.3$ nm (a) PM monolayer imaged in 0.083 µm liquid where the lower part of the sample was pre-radiated in STEM-mode by acquiring the first 50 frames using $\tau = 1$ µs ($D_e = 0.46$ e$^-$Å^{-2} per frame) and then 2 frames with $\tau = 20$ ($D_e = 9.3$ e$^-$Å^{-2} per frame). The final image is shown in and acquired using $\tau = 20$ where arrowheads point to partially removed PMs. (b) PMs imaged in 650 nm liquid. (c) Bandpass-filtered image of (b), showing the segmented outlines obtained via the developed image processing pipeline. (d) Segmented objects averaged from five successive images at $D_e = 9.3$ (red), 27.9 (green), and 46.5 e$^-$Å^{-2} (blue) in the frames. (e) The size distribution of PM moves toward smaller values as the sample is irradiated, suggesting a gradual degradation of its structure. While no significant change (ns) is observed for $D_e = 9.3$ e$^-$Å^{-2}, a significant change with a probability (P) of 0.0015 (***) is found for $D_e = 18.6$ e$^-$Å^{-2}. (f) Size evolution of PMs in liquid with $t =$ 0.008, 0.083, and 0.63 µm.

A common way to analyze image quality is by measuring the *SNR*. de Jonge et al. used a method based on a line scan to assess the signal intensity at a nanoparticle compared to the background intensity and noise level [41]. Fig. 4b and e show line scans over a selected PM and SiONP, respectively, from which the *FWHM* can be measured as well as the *SNR*. However, this method has a disadvantage because the *SNR* obtained in this way depends on the pixel size and exact location of the line scan. Moreover, the low *SNR* leads to inaccuracy in the measurement of the *FWHM*. We describe a new approach based on probing the signal at the nanoparticle as well as the background independent of pixel size.

The key question here is how the *SNR* can be used to quantitatively determine the visibility of a multi-pixel object in order to evaluate the experimental resolution independent of the pixel size used. Images are two-dimensional (2D) arrays of pixels, where each pixel represents the strength of the signal on a lateral scale. It is useful to distinguish between the case of a single-pixel object and a multiple-pixel object, also termed lesion [42]. For a single-pixel object, the signal S_O is surrounded by a noisy background of mean intensity of $\overline{S}_B$. The *SNR* is given by:

$$SNR_O = \frac{S_O - \overline{S}_B}{\sigma_B}, \tag{9}$$

with σ_B the standard deviation of the background signal. The average *SNR* of a pixel in a lesion consisting of n pixels is:

$$\overline{SNR}_L = \frac{\overline{S}_L - \overline{S}_B}{\sqrt{\sigma_L^2 + \sigma_B^2}} \tag{10}$$

In the case of a background level comparable to the signal level, which is typically the case in LP-EM, it can be assumed that $\sigma_L = \sigma_B$, so that:

$$\overline{SNR}_L = \frac{\overline{S}_L - \overline{S}_B}{\sigma_B\sqrt{2}} \tag{11}$$

In order to measure $\overline{S}_L$ directly from the image data, we define circular regions of interest (ROI) with a diameter equal to the FWHM determined above (Fig. 4a and d). $\overline{S}_B$, and σ_B are measured from areas where no particles are present and that represent approximately the same t as where the $\overline{S}_L$ is measured (Fig. 4a and d).

The Rose criterion [43] states that for a single pixel object to be visible from the background, its minimum *SNR* should be 3–5. For a lesion to be visible, the average $\overline{SNR}_L$ can be smaller; this is because the statistical chance to observe a number of adjacent pixels with a slightly different signal than the background makes the lesion observable, even though for an single-pixel object the same *SNR* would be insufficient to recognize it. So, we define an effective *SNR* that expresses the visibility of a multi-pixel object:

$$SNR_L^* = \frac{\overline{S}_L - \overline{S}_B}{\overline{\sigma_B}\sqrt{2}} \tag{12}$$

To derive the relation between SNR_L^* and $\overline{SNR}_L$, a binning operation is used to transform the multi-pixel object into a single-pixel object as described in the following. During the operation, $\overline{S}_L$ and $\overline{S}_B$ stay constant, but $\overline{\sigma_B}$ decreases as we average over n pixels. This becomes clear from looking at the variance, which is the square of the standard deviation:

$$Var(S_B) = \sigma_B^2 \tag{13}$$

During the binning operation, the mean-variance of S_B becomes:

$$Var(S_B)^{mean} = Var\left(\frac{1}{n}\sum_{i=1}^{n} S_{B,i}\right) \tag{14}$$

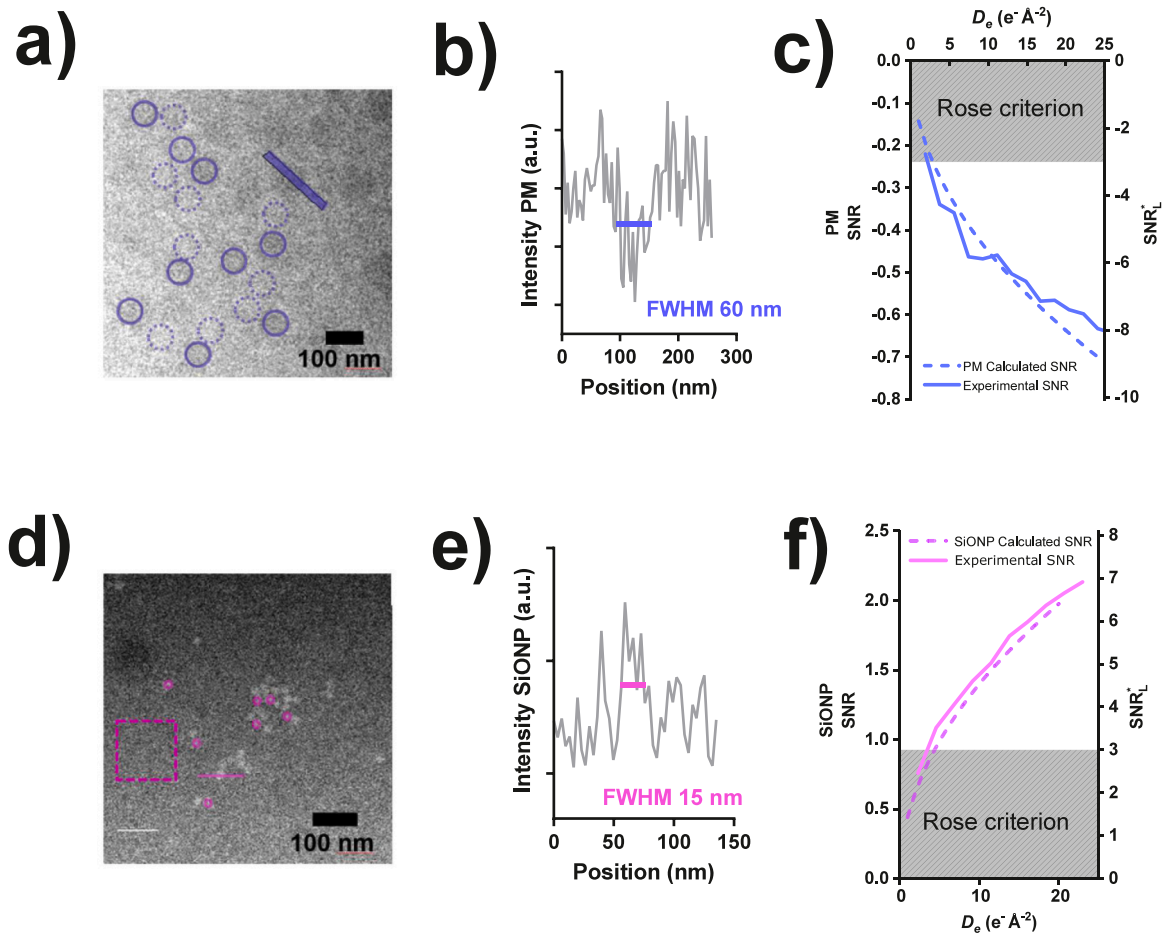

Fig. 4. Defining the signal for direct comparison of experimental and numerically calculated signal to noise ratio (*SNR)* for polystyrene microspheres (PMs; a–c) and silica nanoparticles (SiONPs; d–f) in a liquid cell. (a) PMs immobilized on the upper window imaged using $D_e = 48.2$ e$^-$Å^{-2}. (b) Line profile plot (5 pixels wide) of the line shown in (a) over a single PM, highlighting the full width at half maximum (FWHM). (c) Average experimental *SNR* and SNR_L* (Eq. (17)) as a function of cumulative D_e along with the *SNR* obtained from analytical calculations. Grayed area indicates where SNR_L* does not satisfy the Rose criterion (Eq. (18)). (d) SiONPs imaged at $D_e = 19$ e$^-$Å^{-2}. (e) Line profile plot (2 pixels wide) of the line shown in (d) over a single SiONP, highlighting the FWHM. (f) As (c), for SiONPs.

If it is assumed that each $S_{B,i}$ is a truly random variable (random noise) such that the covariance of any two pixels is zero, and the variance between each pixel is equal (Bienaymé-formula), the following holds:

$$\sqrt{Var\,(S_B)^{mean}} = \sqrt{\frac{1}{n}Var(S_B)}, \tag{15}$$

which yields:

$$\overline{\sigma_B} = \frac{1}{\sqrt{n}}\sigma_B \tag{16}$$

Substitution into Eq. (12) yields:

$$SNR_L^* = \frac{\overline{S}_L - \overline{S}_B}{\sigma_B\sqrt{2}}\sqrt{n} = \overline{SNR}_L\sqrt{n} \tag{17}$$

In terms of visibility of a single object according to the Rose criterion:

$$SNR_L^* \geq 3 \tag{18}$$

We analyze the experimental data using this new method to determine SNR^*_L. The data of the first frame was corrupted and therefore excluded from calculations. In the case of PMs, the area of the signal is specified by placing 60 nm-diameter, spherical ROIs in the middle of PMs that reside 2.4 ± 0.6 μm from the edge of the window, where t = 0.63 μm. This measurement is repeated for 14 PMs. To measure the local intensity and standard deviation of the background for each PM, we also place 14, 60 nm-diameter ROIs just outside of the particles and calculate the corresponding *SNR* for each PM. This allows us to determine the average *SNR* for $N = 14$ particles for the entire image series as a function of D_e was obtained (Fig. 4c). The experimental result can be used for comparison with other experiments using different microscope settings since the *SNR* is independent of pixel size (and magnification). Fig. 4c also includes the numerically calculated *SNR* (Eq. (4)) for comparison. As can be seen, the negative contrast is correctly predicted by the analytical model.

To measure the average *SNR* of SiONPs, 24 particles are selected at a distance of 0.95 ± 0.05 μm from the edge of the window, which corresponds to a t of 0.35 μm. For the analysis of the *SNR*, we define spherical ROIs with a 15 nm diameter centered on each selected particle (Fig. 4d). To measure the average intensity of the standard deviation of the background signal, an 880 × 90 nm^2 rectangular ROI is created with an area of 0.079 μm^2. The average *SNR* value for SiONPs in 350 nm of liquid is calculated according to Eq. (9). Fig. 4f shows the obtained experimental *SNR* versus D_e and the comparison with the calculated values.

Finally, to estimate the minimum D_e required to successfully distinguish a PM or SiONP in these experimental conditions, the value of SNR_L* was calculated using Eq. (17) and setting $N = 316$ (PMs) or N = 21 (SiONPs) corresponding to the number of analyzed pixels within the 60 nm and 15 nm ROIs, respectively. These values are indicated by the right y-axes in Fig. 4c and f. For PM, approximately 2.5 e$^-$Å^{-2} is required to distinguish a single particle, while for SiONP, a dose of 5 e$^-$Å^{-2} is

needed. Here, excellent agreement between experiment and theory is obtained as is shown in Fig. 4c and f. This approach can thus be used to predict LP-EM image quality for low-Z materials at low D_e, as needed to optimize experimental parameters.

3.4. Imaging pre-formed binary structures

With optimized experimental settings, we set out to resolve the structural detail of self-organized binary structures in STEM mode. These structures are synthesized by mixing PMs and SiONPs before measurements. A typical overview image of the sample is shown in Fig. 5a, where structures of varying contrast are visible. Lower-contrast structures often disappear from the field of view upon prolonged electron beam irradiation; some of these structures are highlighted in Fig. 5a. The dynamics of one such structure is captured by recording a sequence of 32 frames with $D_e = 0.46 \pm 0.05$ $e^{-}Å^{-2}$ per frame and a frame rate of 1.66 frames per second. This recording results in a video where binary particles initially rotate and then suddenly disappear from the field of view, leaving behind a few SiONPs attached to the liquid-solid interface. The behavior of these binary structures in the liquid is shown in Fig. 5b, where three STEM frames from the video are shown at time points 1.2, 18, and 36 s. High-contrast structures typically remain stationary upon electron beam irradiation. After the LP-EM experiment, the cell is opened, and both windows are inspected using SEM. On the bottom window, particles are found on both sides, indicating that the bright structures in Fig. 5a are dried deposits of binary suspension leaking to this side of the window during loading.

Finally, in Fig. 5c, eight first frames of the video are manually aligned and averaged, resulting in D_e of 4 ± 0.4 $e^{-}Å^{-2}$. The image reveals the raspberry-type structure, while some of the binary particles are slightly blurred because of their movement. Based on the analysis of three videos taken at different locations of the same sample, we found that on average 50% of the binary particles (N=50) have detached from the SiN-membrane at D_e=*10* $\pm$ *5* $e^{-}Å^{-2}$. These results highlight that it is feasible to observe a dynamic process occurring in this soft-matter structure below the threshold D_e for radiation damage while the motion of nano-objects might become the resolution-limiting factor.

4. Discussion

Since LP-EM experiments are notoriously difficult to conduct and time-consuming, it is beneficial to limit the number of experiments by first analyzing relevant parameters *in silico*. The spatial resolution can be improved for fixed D_e by optimizing β to obtain the maximum possible contrast. Optimization of β is of particular importance for BF detection in STEM, while it is sufficient for DF-STEM to set β above a certain minimum value due to the flat shape of the d_{min} vs β curve. As the resolution is critically sensitive to the density of the nano-object, precise

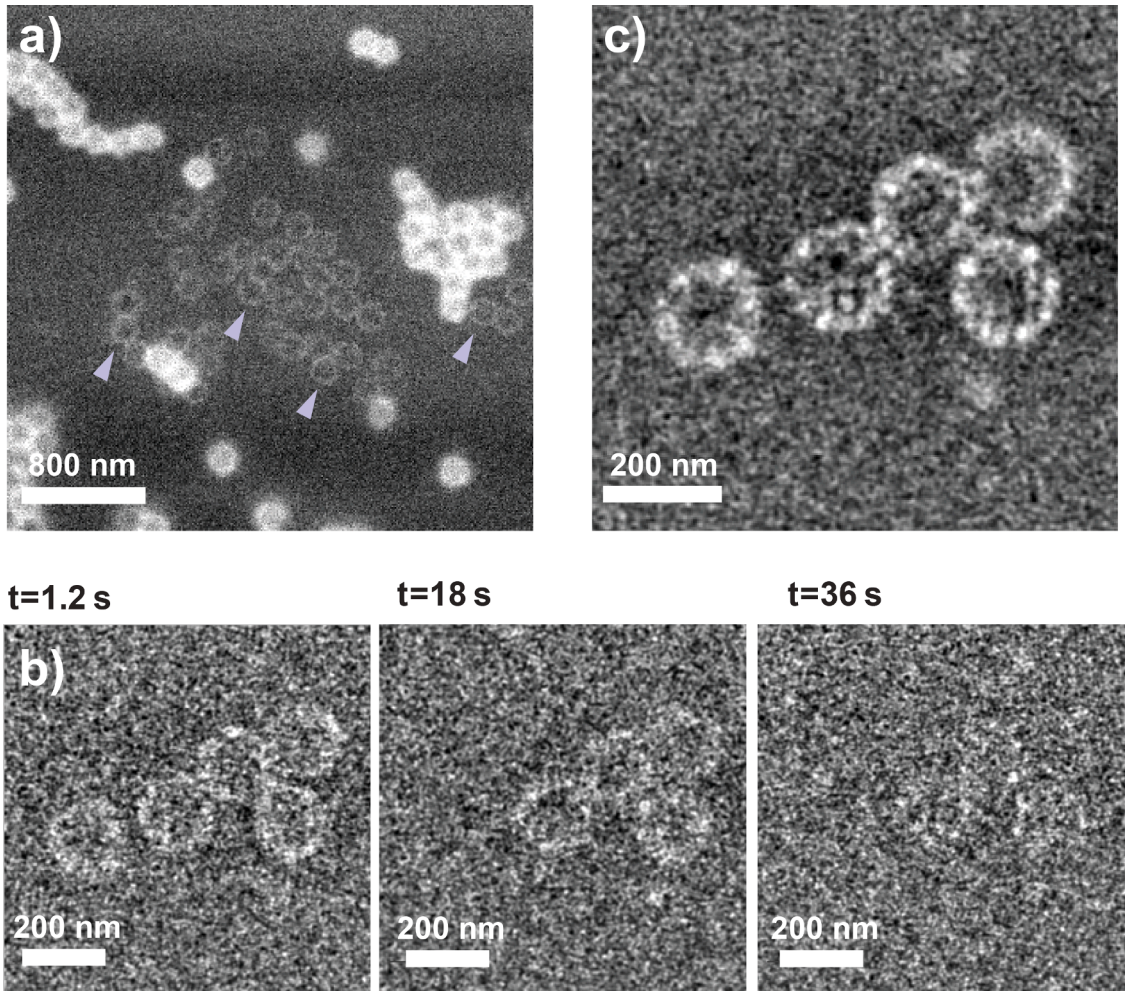

Fig. 5. Imaging the structure and dynamics of binary particles in a liquid cell with DF-STEM. (a) Overview image of a liquid cell experiment showing immersed binary structures highlighted with blue arrowheads ($s = 10$ nm and $\tau = 20$ µs). (b) Image sequence showing gradual detachment or degradation of binary structures from the liquid-solid interface, leaving a few SiONPs behind. Images in the sequence were acquired with $\beta = 54$ mrad, $s = 3.3$ nm, and $\tau = 1$ µs in $t = 500$–600 nm liquid with $D_e = 0.46$ $e^{-}Å^{-2}$ per frame resulting in a frame time of 1.2 s. (c) Average of 8 aligned frames showing the characteristic raspberry structure as resolved using $D_e = 4$ $e^{-}Å^{-2}$.

calculations require its value to be determined within a small error margin, which is not always possible in practice. This issue needs to be considered when comparing experimental data with calculated values. For correct estimates of the material's properties, we find an excellent agreement between the calculated and experimental *SNR*.

When radiation-sensitive low-Z material is studied in liquid, the resolution is *SNR*-limited, implying that the distinguishability of a nano-object is a stochastic matter. It is not always clear how to optimize the microscope settings for maximum *SNR* at the lowest possible D_e, since *SNR* depends on *s*, which means that *SNR* varies with microscope magnification. For the study of spherical nano-objects, we, therefore, propose to determine $\overline{SNR}_L$ by measuring the average *SNR* in a lesion consisting of *n* pixels (Eq. (10)). What is compared is a lesion over the object of interest and a lesion of the same size over the background. The starting point is the minimum magnification for detection at $d_{\min} = 2s$. In case the objects show $\overline{SNR}_L > 3$, a smaller *s* can be applied in STEM image acquisition to resolve finer details of the objects. Here, it should be mentioned that the calculated resolution applies only to SiONPs residing in a single layer. In the case of more complex structures, the effective resolution may change at locations with overlapping particles in the image projection.

Ideally, an acceptable electron dose or fluence should be determined for each component of the sample in liquid. In practice, this can be difficult, as structural changes may occur at multiple length scales [18]; perhaps not all are accessible by the microscopic system used. The structure of SiONP was found to stay intact for the tested $D_e < 25\ e^{-}Å^{-2}$, consistent with earlier reports of particle elongation at cumulative $D_e = 10^3$–$10^4\ e^{-}Å^{-2}$ [27]. We did not address potential damage to the functionalization at the SiONP's surface [44], which could affect assembly properties.

When PMs were imaged in a vacuum, no structural changes were observed. However, the projected diameter of PMs shrank when irradiated in a liquid cell containing ambient air or aqueous solution. A statistically significant reduction of the diameter of PM was observed at a cumulative D_e above $D_e = 18.6 \pm 2\ e^{-}Å^{-2}$, which is somewhat below of damage threshold reported by others [26]. It should be noted that our method of defining the acceptable D_e is a method for observing the result of electron beam damage at the scale of the nanoobject but it does not directly probe the damage at the atomic scale. In addition, the sensitivity of the method depends on the detection efficiency, whereby more sensitive detection than what is used here, would possibly reveal small changes in the diameter of the PM not visible in our experiment. Other methods known in literature for assessing the limit of radiation involve, for example, measuring changes in the chemical composition of the object [45], and observation of fragmentation of a polymer [46]. To qualitatively explain the observed structural degradation of the PMs, we hypothesize a combination of direct and indirect damage where the electron beam disrupts the PM's polymer backbone, and creates free radicals in the surroundings that damage the structure from the outside [45], which leads to depolymerization and subsequent structural degradation of the PMs. Another possibility for the observed degradation is that the oxidized PM structure becomes hydrophilic and swells as water enters the structure [46]. Increasing water content and formation of gel-like substance could result in a diminishing contrast of PMs, which in turn, could be interpreted as degradation.

The hierarchical structure of binary particles was directly visualized using a STEM low-dose imaging protocol that allowed setting a balance between sufficient *SNR* and temporal resolution in the post-processing step of the data while staying within the electron beam damage limit. When irradiated with the STEM probe, the binary structures detached from the windows surface at $D_e > 20\ e^{-}Å^{-2}$. No degradation was observed within this range of D_e, and the limiting factor for resolving the hierarchical binary structure was motion blur. This movement could be due to secondary electrons charging the SiN_x-membrane [47]. Another possibility is that the pH and ionic strength [48] change due to the radiolysis products that are formed in the irradiated liquid volume. The increased ionic strength may lead to the screening of electrostatic charges [44] that promote the attachment of particles on the window surface in the first place. Also, beam-induced changes in the pH could change the interaction potential between the siloxane-terminated SiN_x-surface [49] and amino-terminated SiONPs.

Finally, it is important to consider what complementary information LP-EM provides compared to dry-state and cryo-EM. When imaging the binary core-shell structure in a dry state, we commonly observe that many of the structures have collapsed, likely due to the capillary effect that disrupts the shell during the drying process [50]. In a recent cryo-EM study [51], the binary structure was imaged as embedded in vitreous ice, and it was possible to obtain a 3D-reconstruction of the SiONP distribution in the shell surrounding the PM core. Our LP-EM study shows that the shell retains its shape during sample preparation, but resolving the location of each individual SiONP is impossible due to the movement of the particles. It thus seems that the sample preparation in LP-EM is also able to preserve the binary structure intact so that the hierarchical binary structure could be observed. However, the image quality in sample thicknesses optimized for dynamic studies is inferior when compared with results from cryo-EM, where the sample is thinner, windows are absent, and higher electron doses can be used resulting in detection with higher resolution [29].

For maximal electron efficiency, it might be therefore beneficial to enable phase-contrast imaging by switching to TEM-mode and minimizing the liquid thickness to a level where phase-contrast effects become prominent [52]. For best observations, the PMs would need to be fixed to the SiN surface thus enhancing the observation of SiONP dynamics. Their mobility could be potentially tuned by unspecific [15] or specific [53] modification of the SiN surface. Earlier, it has been shown that the TEM illumination mode can be better for keeping particles adhered to the membrane [52]. Faster imaging and computation will also help observe motion [12]. Electron damage can possibly be mitigated in this type of experiment by using chemical additives [54], and using graphene to materials in the construction of the liquid cell [55].

5. Conclusions

We show how a combination of theoretical calculations and experiments can be used to examine which parameters have the most influence and need optimization to achieve optimal resolution in LP-EM studies of beam-sensitive and low-contrast nano-objects. In addition to experimental parameters *t*, D_e, and β, information about the exact density of the nano-object is crucial. For the experimental setup considered, DF-STEM is preferred over BF-STEM because it has similar performance and its image resolution is less sensitive to the detector opening angle settings. In addition, DF-STEM allows the identification of the different components of the sample via negative contrast on PMs. The theory of noise-limited resolution is based on the *SNR* of a single-pixel level at the center of a nano-object via the Rose criterion. In acquired data, however, nano-objects typically occupy several pixels. To precisely calculate the detectability of such nano-objects, we introduced SNR^*_L, which is proportional to the square root of the number of pixels involved. Electron beam illumination of the sample may result in physical and chemical changes to the sample, and it is, therefore, crucial to understand what impact the delivered D_e will have on the acquired data. A method was introduced that relies on a statistical analysis of morphological changes in the image data, and a maximal D_e was determined below which radiation damage was tolerable. It was thus possible to visualize beam-sensitive, hierarchical low-Z binary structures consisting of SiONPs and PMs, and recognize both components. The optimization method introduced here may also find application in LP-EM studies of other radiation-sensitive and low-Z materials.

Declaration of Competing Interest

The authors declare that they have no known competing financial interests or personal relationships that could have appeared to influence the work reported in this paper.

Data availability

Data will be made available on request.

Acknowledgments

The authors like to thank Sebastian Rzadkiewicz for synthesizing the SiONPs and for discussions, Xufen Xu and Deniz Eren for discussions about the density and zeta potential of colloidal particles used in this work, Isabella Tavernano for measuring the zeta potential of SiONP dispersion, Hanglong Wu for the help with initial LP-EM experiments, and Joe Patterson for discussions and advice on LP-EM experiments. We thank Eduard Arzt for his support through INM and acknowledge funding by the Marie Sklodowska-Curie ITN project MULTIMAT.

Supplementary materials

Supplementary material associated with this article can be found, in the online version, at doi:10.1016/j.ultramic.2022.113596.

References

[1] B.H. Kim, J. Yang, D. Lee, B.K. Choi, T. Hyeon, J. Park, Liquid-phase transmission electron microscopy for studying colloidal inorganic nanoparticles, Adv. Mater. 30 (2018).
[2] S.F. Tan, S.W. Chee, G. Lin, U. Mirsaidov, Direct observation of interactions between nanoparticles and nanoparticle self-assembly in solution, Acc. Chem. Res. 50 (2017) 1303.
[3] H. Wu, H. Friedrich, J.P. Patterson, N. Sommerdijk, N. de Jonge, Liquid-phase electron microscopy for soft matter science and biology, Adv. Mater. 32 (2020), 2001582.
[4] H.M. Zheng, S.A. Claridge, A.M. Minor, A.P. Alivisatos, U. Dahmen, Nanocrystal diffusion in a liquid thin film observed by *in situ* transmission electron microscopy, Nano Lett. 9 (2009) 2460.
[5] E.A. Ring, N. de Jonge, Microfluidic system for transmission electron microscopy, Microsc. Microanal. 16 (2010) 622.
[6] E.A. Ring, N. de Jonge, Video-frequency scanning transmission electron microscopy of moving gold nanoparticles in liquid, Micron 43 (2012) 1078.
[7] L.R. Parent, E. Bakalis, M. Proetto, Y.W. Li, C. Park, F. Zerbetto, N.C. Gianneschi, Tackling the challenges of dynamic experiments using liquid-cell transmission electron microscopy, Acc. Chem. Res. 51 (2018) 3.
[8] A.S. Powers, H.G. Liao, S.N. Raja, N.D. Bronstein, A.P. Alivisatos, H. Zheng, Tracking nanoparticle diffusion and interaction during self-assembly in a liquid cell, Nano Lett. 17 (2017) 15.
[9] H. Wang, X. Zhou, Y. Huang, X. Chen, C. Jin, Interactions of sub-five-nanometer diameter colloidal palladium nanoparticles in solution investigated via liquid cell transmission electron microscopy, RSC Adv. 10 (2020) 34781.
[10] A. Verch, M. Pfaff, N. De Jonge, Exceptionally slow movement of gold nanoparticles at a solid/liquid interface investigated by scanning transmission electron microscopy, Langmuir 31 (2015) 6956.
[11] G. Lin, X. Zhu, U. Anand, Q. Liu, J. Lu, Z. Aabdin, H. Su, U. Mirsaidov, Nanodroplet-mediated assembly of platinum nanoparticle rings in solution, Nano Lett. 16 (2016) 1092.
[12] T.A.J. Welling, S. Sadighikia, K. Watanabe, A. Grau-Carbonell, M. Bransen, D. Nagao, A. van Blaaderen, M.A. van Huis, Observation of undamped 3D brownian motion of nanoparticles using liquid-cell scanning transmission electron microscopy, Part. Part. Syst. Charact. 37 (2020), 2000003.
[13] M.W.P. van de Put, C.C.M.C. Carcouët, P.H.H. Bomans, H. Friedrich, N. de Jonge, N.A.J.M. Sommerdijk, Writing silica structures in liquid with scanning transmission electron microscopy, Small 11 (2015) 585.
[14] L.R. Parent, E. Bakalis, A. Ramírez-Hernández, J.K. Kammeyer, C. Park, J. de Pablo, F. Zerbetto, J.P. Patterson, N.C. Gianneschi, Directly observing micelle fusion and growth in solution by liquid-cell transmission electron microscopy, J. Am. Chem. Soc. 139 (2017) 17140.
[15] J.P. Patterson, P. Abellan, M.S. Denny, C. Park, N.D. Browning, S.M. Cohen, J. E. Evans, N.C. Gianneschi, Observing the growth of metal-organic frameworks by *in situ* liquid cell transmission electron microscopy, J. Am. Chem. Soc 137 (2015) 7322.
[16] M.N. Yesibolati, K.I. Mortensen, H. Sun, A. Brostrøm, S. Tidemand-Lichtenberg, K. Mølhave, Unhindered brownian motion of individual nanoparticles in liquid phase scanning transmission electron microscopy, Nano Lett. 20 (10) (2020) 7108–7115, https://doi.org/10.1021/acs.nanolett.0c02352.
[17] J. Hermannsdörfer, N. de Jonge, A. Verch, Electron beam induced chemistry of gold nanoparticles in saline solution, Chem. Commun. 51 (2015) 16393.
[18] S. Keskin, N. de Jonge, Reduced radiation damage in transmission electron microscopy of proteins in graphene liquid cells, Nano Lett. 18 (2018) 7435.
[19] K. Gnanasekaran, H. Chang, P.J.M. Smeets, J. Korpanty, F.M. Geiger, N. C. Gianneschi, *In situ* Ni^{2+} stain for liposome imaging by liquid-cell transmission electron microscopy, Nano Lett. 20 (2020) 4292.
[20] P. Abellan, T.J. Woehl, L.R. Parent, N.D. Browning, J.E. Evans, I. Arslan, Factors influencing quantitative liquid (scanning) transmission electron microscopy, Chem. Commun. 50 (2014) 4873.
[21] Y. Tomo, K. Takahashi, T. Nishiyama, T. Ikuta, Y. Takata, Nanobubble nucleation studied using Fresnel fringes in liquid cell electron microscopy, Int. J. Heat Mass Transf. 108 (2017) 1460.
[22] H. Wu, H. Friedrich, J.P. Patterson, N.A.J.M. Sommerdijk, N. de Jonge, Liquid-phase electron microscopy for soft matter science and biology, Adv. Mater. 32 (25) (2020), 2001582.
[23] M.A. Moradi, D. Eren, S. Rzadkievics, A. Keizer, M.M.J. van Rijt, P.H.H. Bomans, H. Friedrich, N.A.J.M. Sommerdijk, J.P. Patterson, Formation of hierarchical hybrid silica-polymer using quantitative cryo- electron tomography, Microsc. Microanal. 25 (2019) 59.
[24] M. Bardosova, M.E. Pemble, I.M. Povey, R.H. Tredgold, The langmuir-blodgett approach to making colloidal photonic crystals from silica spheres, Adv. Mater. 22 (2010) 3104.
[25] Z. Li, S. Das, P. Hongmanorom, N. Dewangan, M.H. Wai, S. Kawi, Silica-based micro- and mesoporous catalysts for dry reforming of methane, Cat. Sci. Technol. 8 (2018) 2763.
[26] K. Varlot, J.M. Martin, C. Quet, Physical and chemical changes in polystyrene during electron irradiation using EELS in the TEM: contribution of the dielectric function, J. Microsc. 191 (1998) 187.
[27] J. Zečević, J. Hermannsdörfer, T. Schuh, K.P. de Jong, N. de Jonge, Anisotropic shape changes of silica nanoparticles induced in liquid with scanning transmission electron microscopy, Small 13 (2017), 1602466.
[28] K. Gnanasekaran, G. de With, H. Friedrich, Quantification and optimization of ADF-STEM image contrast for beam-sensitive materials, Roy. Soc. Open Sci. 5 (2018), 171838.
[29] N. de Jonge, Theory of the spatial resolution of (scanning) transmission electron microscopy in liquid water or ice layers, Ultramicroscopy 187 (2018) 113.
[30] T. Yokoi, Y. Sakamoto, O. Terasaki, Y. Kubota, T. Okubo, T. Tatsumi, Periodic arrangement of silica nanospheres assisted by amino acids, J. Am. Chem. Soc. 128 (2006) 13664.
[31] G.T. Hermanson, Bioconjugate Techniques, 2nd ed, Elsevier, Amsterdam, 2013.
[32] D.B. Williams, C.B. Carter, Lenses, Apertures, and Resolution, in: D.B. Williams, C. B. Carter (Eds.). Transmission Electron Microscopy: A Textbook for Materials Science 32, Springer US, 2009, p. 91.
[33] E.A. Ring, D.B. Peckys, M.J. Dukes, J.P. Baudoin, N. de Jonge, Silicon nitride windows for electron microscopy of whole cells, J. Microsc. 243 (2011) 273.
[34] S. Keskin, P. Kunnas, N. de Jonge, Liquid-phase electron microscopy with controllable liquid thickness, Nano Lett. 19 (2019) 4608.
[35] H. Wu, H. Su, R.R.M. Joosten, A.D.A. Keizer, L.S. van Hazendonk, M.J.M. Wirix, J. P. Patterson, J. Laven, G. de With, H. Friedrich, Mapping and controlling liquid layer thickness in liquid-phase (scanning) transmission electron microscopy, Small Meth. 5 (2021), 2001287.
[36] T. Malis, S.C. Cheng, R.F. Egerton, EELS log-ratio technique for specimen-thickness measurement in the TEM, J. Electron. Microsc. Technol. 8 (1988) 193.
[37] K.L. Jungjohann, J.E. Evans, J.A. Aguiar, I. Arslan, N.D. Browning, Atomic-scale imaging and spectroscopy for *in situ* liquid scanning transmission electron microscopy, Microsc. Microanal. 18 (2012) 621.
[38] J.M. Yuk, J. Park, P. Ercius, K. Kim, D.J. Hellebusch, M.F. Crommie, J.Y. Lee, A. Zettl, A.P. Alivisatos, High-resolution EM of colloidal nanocrystal growth using graphene liquid cells, Science 336 (2012) 61.
[39] M. Textor, N. de Jonge, Strategies for preparing graphene liquid cells for transmission electron microscopy, Nano Lett. 18 (2018) 3313.
[40] X. Xu, T. Franke, K. Schilling, N.A.J.M. Sommerdijk, H. Cölfen, Binary colloidal nanoparticle concentration gradients in a centrifugal field at high concentration, Nano Lett. 19 (2019) 1136.
[41] N. de Jonge, N. Poirier-Demers, H. Demers, D.B. Peckys, D. Drouin, Nanometer-resolution electron microscopy through micrometers-thick water layers, Ultramicroscopy 110 (2010) 1114.
[42] Q. Bao, A.F. Chatziioannou, Estimation of the minimum detectable activity of preclinical PET imaging systems with an analytical method, Med. Phys. 37 (2010) 6070.
[43] A. Rose, Comparative noise properties of vision, television, and photographic film, in: A. Rose (Ed.). Vision: Human and Electronic, Springer US, 1973.
[44] J. Kim, M.R. Jones, Z. Ou, Q. Chen, *In Situ* electron microscopy imaging and quantitative structural modulation of nanoparticle superlattices, ACS Nano 10 (2016) 9801.
[45] K. Donald, Beam damage of polypropylene in the environmental scanning electron microscope: an FTIR study, J. Microsc. 190 (1998) 357.
[46] M.A. Touve, A.S. Carlini, N.C. Gianneschi, Self-assembling peptides imaged by correlated liquid cell transmission electron microscopy and MALDI-imaging mass spectrometry, Nat. Commun. 10 (2019) 4837.
[47] T.J. Woehl, T. Prozorov, The mechanisms for nanoparticle surface diffusion and chain self-assembly determined from real-time nanoscale kinetics in liquid, J. Phys. Chem. C 119 (2015) 21261.

[48] N.M. Schneider, M.M. Norton, B.J. Mendel, J.M. Grogan, F.M. Ross, H.H. Bau, Electron-Water interactions and implications for liquid cell electron microscopy, J. Phys. Chem. C 118 (2014) 22373.
[49] J.R. Dwyer, Y.M.N.D.Y. Bandara, J.C. Whelan, B.I. Karawdeniya, J.W. Nichols, Chapter 7. Silicon Nitride Thin Films for Nanofluidic Device Fabrication (2016) 190–236. https://doi.org/10.1039/9781849735230-00190.
[50] S.S.W. Tai, X.M. Tang, Manipulating biological samples for environmental scanning electron microscopy observation, Scanning 23 (2001) 267.
[51] M.A. Moradi, E.D. Eren, M. Chiappini, S. Rzadkiewicz, M. Goudzwaard, M.M.J. van Rijt, A.D.A. Keizer, A.F. Routh, M. Dijkstra, G. de With, N. Sommerdijk, H. Friedrich, J.P. Patterson, Spontaneous organization of supracolloids into three-dimensional structured materials, Nat. Mater. 20 (4) (2021) 541–547.
[52] S. Keskin, P. Kunnas, N. de Jonge, Liquid-phase electron microscopy with controllable liquid thickness, Nano Lett. 19 (2019) 4608.
[53] A.W. Robertson, G. Zhu, B.L. Mehdi, R.M.J. Jacobs, J. De Yoreo, N.D. Browning, Nanoparticle immobilization for controllable experiments in liquid-cell transmission electron microscopy, ACS Appl. Mater. Interfaces 10 (2018) 22801.
[54] T.J. Woehl, P. Abellan, Defining the radiation chemistry during liquid cell electron microscopy to enable visualization of nanomaterial growth and degradation dynamics, J. Microsc. 265 (2017) 135.
[55] H. Cho, M.R. Jones, S.C. Nguyen, M.R. Hauwiller, A. Zettl, A.P. Alivisatos, The use of graphene and its derivatives for liquid-phase transmission electron microscopy of radiation-sensitive specimens, Nano Lett. 17 (2017) 414.